10-11-2018

Conforming nanoparticle sheets to surfaces with Gaussian curvature

Noah P. Mitchell

Remington L. Carey

Jelani Hannah

Yifan Wang

Sean P. McBride
Marshall University, mcbrides@marshall.edu

See next page for additional authors

Recommended Citation
Mitchell, N. P., Carey, R. L., Hannah, J., Wang, Y., Ruiz, M. C., McBride, S. P., ... & Jaeger, H. M. (2018). Conforming nanoparticle sheets to surfaces with Gaussian curvature. Soft Matter, 14(45), 9107-9117.

Authors
Noah P. Mitchell, Remington L. Carey, Jelani Hannah, Yifan Wang, Sean P. McBride, Xiao-Min Lin, and Heinrich M. Jaeger

Conforming nanoparticle sheets to surfaces with Gaussian curvature

Noah P. Mitchell,[1,*] Remington L. Carey,[1,2,†] Jelani Hannah,[1] Yifan Wang,[1,3] Maria Cortes Ruiz,[1] Sean McBride,[1,4] Xiao-Min Lin,[5] and Heinrich M. Jaeger[1,‡]

[1] *James Franck Institute and Department of Physics, University of Chicago, Chicago, IL, USA*
[2] *Cavendish Laboratory, University of Cambridge, Cambridge, UK*
[3] *Division of Engineering and Applied Science, California Institute of Technology, Pasadena, CA, USA*
[4] *Marshall University, Huntington, WV, USA*
[5] *Center for Nanoscale Materials, Argonne National Laboratory, Argonne, Illinois, USA*

Nanoparticle monolayer sheets are ultrathin inorganic-organic hybrid materials that combine highly controllable optical and electrical properties with mechanical flexibility and remarkable strength. Like other thin sheets, their low bending rigidity allows them to easily roll into or conform to cylindrical geometries. Nanoparticle monolayers not only can bend, but also cope with strain through local particle rearrangement and plastic deformation. This means that, unlike thin sheets such as paper or graphene, nanoparticle sheets can much more easily conform to surfaces with complex topography characterized by non-zero Gaussian curvature, like spherical caps or saddles. Here, we investigate the limits of nanoparticle monolayers' ability to conform to substrates with Gaussian curvature by stamping nanoparticle sheets onto lattices of larger polystyrene spheres. Tuning the local Gaussian curvature by increasing the size of the substrate spheres, we find that the stamped sheet morphology evolves through three characteristic stages: from full substrate coverage, where the sheet extends over the interstices in the lattice, to coverage in the form of caps that conform tightly to the top portion of each sphere and fracture at larger polar angles, to caps that exhibit radial folds. Through analysis of the nanoparticle positions, obtained from scanning electron micrographs, we extract the local strain tensor and track the onset of strain-induced dislocations in the particle arrangement. By considering the interplay of energies for elastic and plastic deformations and adhesion, we construct arguments that capture the observed changes in sheet morphology as Gaussian curvature is tuned over two orders of magnitude.

While any flat thin sheet can easily be rolled into a cylinder, common experience suggests that conforming the same sheet to a sphere is considerably more difficult. In order to accommodate the curvature of the sphere, one must fold, cut, or stretch the sheet. On surfaces with Gaussian curvature — that is, curvature in two independent directions, such as on a sphere or saddle — triangles no longer have interior angles which sum to 180°. Conforming a flat sheet tightly to such a surface thus necessarily introduces stresses from stretching or compression. If the stresses build up, the material may respond by delaminating, forming cracks or dislocations, or forming folds [1, 2]. For applications where initially flat sheets are to conform to arbitrary surface topographies, the ability to cope with Gaussian curvature therefore translates into a requirement for high bendability combined with an ability to deform locally in-plane, either elastically or plastically.

In close-packed nanoparticle monolayers, individual metallic or semiconducting particle cores are embedded in a matrix of interpenetrating ligand molecules that are attached to each core [3, 4]. This organic matrix largely determines the sheet's mechanical properties. While these properties have been studied for sheets in planar geometries [5–7] and for cylindrical, scroll-like structures [8], the ability of flat sheets to conform to surfaces with Gaussian curvature has received little attention [9]. Here, we investigate this by stamping monolayers of dodecane thiol-ligated gold nanoparticles onto surfaces formed by lattices of larger polystyrene (PS) spheres.

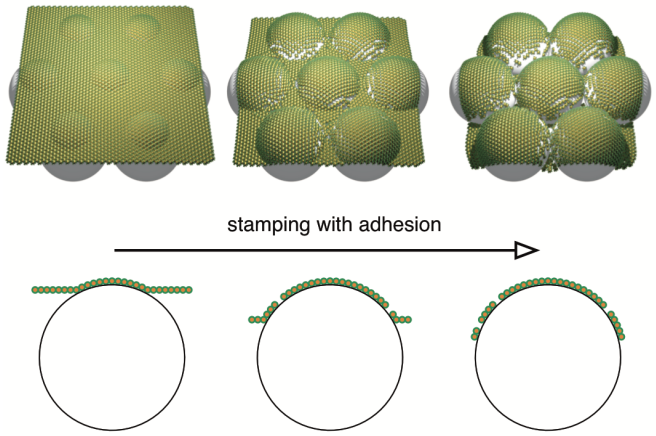

FIG. 1. **Nanoparticle sheets conform to highly curved surfaces.** In the situation under study, a preformed nanoparticle monolayer is pressed against a substrate comprised of a lattice of larger spheres. As the sheet is stamped, the nanoparticles become pinned to the substrate spheres. The three snapshots (top) are from a simulation of an elastic network. As the thin sheet conforms to the substrate while experiencing pinning forces, stresses result in broken bonds between nanoparticles.

The situation we address begins with pre-assembled flat sheets that deform as they are stamped against a highly curved surface, as illustrated in Fig. 1. For

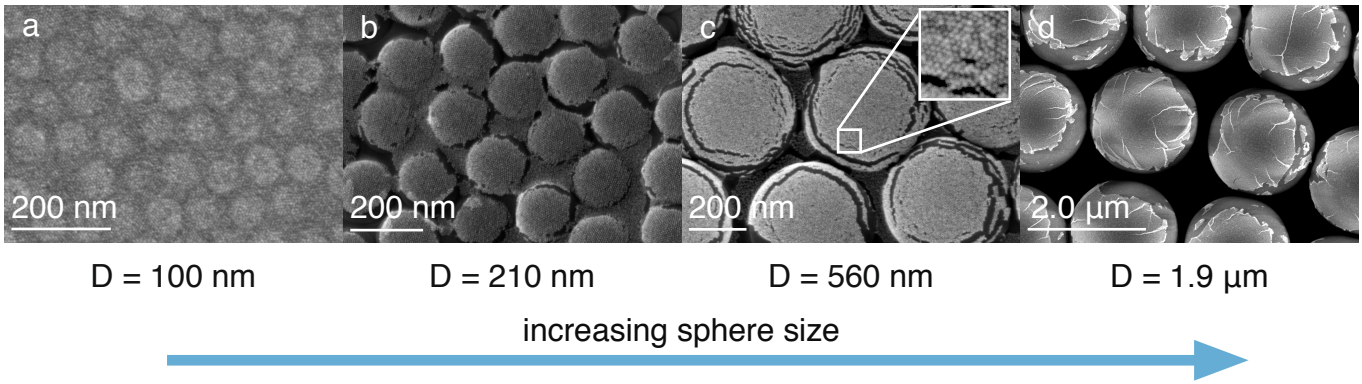

FIG. 2. **Characteristic morphologies of stamped nanoparticle sheets.** (a) At small sphere diameter D, the monolayer sheet is able to cover the polystyrene sphere array completely, but does not fully conform to each sphere. (b-c) As D increases, the sheets tightly conform to the upper portions of the spheres. However, they no longer bridge the crevices between spheres and instead form azimuthal cracks. (d) At even larger D, sheets buckle out of plane, creating radial folds.

nanometer-thin sheets, van der Waals forces generate adhesion that effectively immobilizes the nanoparticles as they come into contact with the substrate. Furthermore, in contrast to continuum elastic sheets, the discrete nanoparticle lattice allows for the formation and proliferation of defects in addition to straining, folding, and fracturing during the conformation process.

The effect of strong pinning to the substrate results in strikingly different behavior than found for the equilibrium arrangement of interacting Brownian particles on spheres [10, 11], frustrated equilibrium conformations of macroscopic, continuum elastic sheets [1, 2], or non-equilibrium growth of colloidal crystals on spherical interfaces [12]. Because the pinned sheet cannot relax to minimize free energy, the effects of geometric frustration build up according to history-dependent, sequential rules. This sequential adhesion gives rise to qualitatively different stress fields in the sheet and suppresses wrinkling before the appearance of sharp folds.

Depending on the local Gaussian curvature, K, of the substrate, which we control by the PS sphere diameter D via $K = 4/D^2$, we find three characteristic stamped-sheet morphologies. As seen in Fig. 2, increasing D leads from sheets that entirely cover the corrugated substrate to sheets that have fractured into caps closely conforming to the top portions of the PS spheres to, finally, even larger caps exhibiting radial folds similar to those seen in macroscopic, continuum sheets [13, 14]. We show that these curvature-dependent morphologies emerge from the interplay between strong pinning to the substrate, elastic energies, and costs for defect formation. This allows us to generate predictions for the conditions required to obtain full coverage and for the limits to which nanoparticle sheets can conform tightly to arbitrarily curved surfaces.

In what follows, we first describe the experiments and resulting sheet morphologies. We then provide energy scaling arguments that predict the crossovers between stamped sheet morphologies as a function of D or K. This is followed by an analysis of direct measurements of the local strain within the stamped sheets, which we compare to simulations of two-dimensional (2D) spring networks made to conform to sphere lattices. From this, we determine the onset of finite size effects due to the discrete nature of the nanoparticles, which alters the continuum prediction for small PS sphere sizes and allows us to predict the maximum polar angle up to which the sheet can tightly conform to individual PS spheres.

EXPERIMENTAL PROCEDURE

Dodecane thiol-ligated gold nanoparticles were synthesized via a digestive ripening method followed by extensive washing with ethanol and finally dissolution in toluene [15]. This process yielded nanoparticles with diameter 5.2 nm and ligand lengths 1.7 nm. Nanoparticle monolayers were self-assembled at the surface of a water droplet. After depositing a drop ($\sim$ 150 μL) of deionized water onto the hydrophobic surface of a piece of PTFE (Bytac), 5-7 μL of the nanoparticle-toluene solution were pipetted around the drop perimeter. The solution climbed to the top of the droplet almost immediately, and, as the toluene evaporated, the nanoparticles self-assembled into a close-packed monolayer with an average lattice spacing of $\approx$ 7.2 nm (Fig. 3a-d). Waiting several hours allowed some of the water to evaporate as well. Given the strong pinning of the drop's contact line to the substrate, this evaporation changed the droplet shape from spherical cap to flattened dome (not shown in Fig. 3b).

At this stage, a silicon chip coated with a lattice of polystyrene (PS) spheres was gently pressed into the assembled monolayer and peeled away (Fig. 3e,f). These PS sphere lattices were created by diluting solutions of PS spheres (Bangs Laboratories) by a factor of 100 using deionized water, then depositing 5-7 μL of the diluted

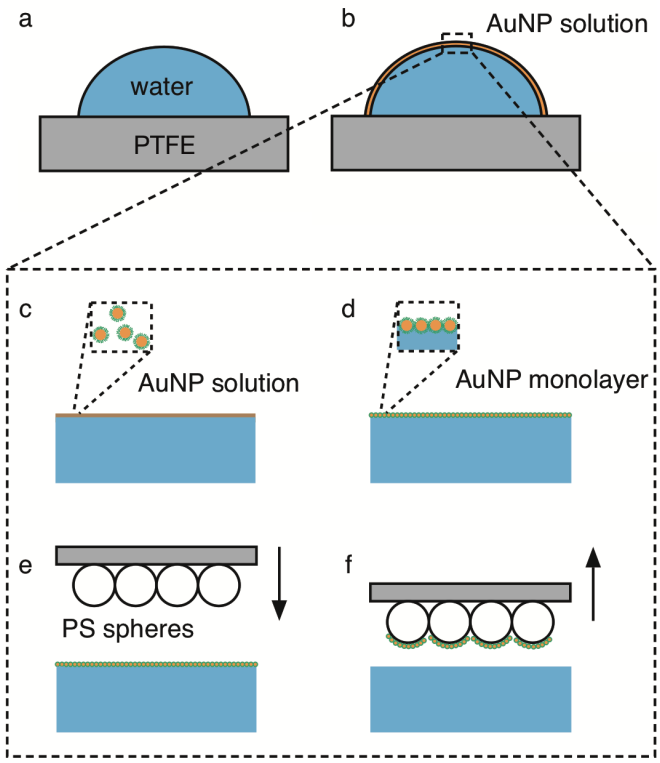

FIG. 3. **Schematic of the experimental procedure for conforming self-assembled gold nanoparticle monolayer sheets to a lattice of polystyrene spheres.** *(a & b)* Drying-mediated assembly of a nanoparticle monolayer at the surface of a water droplet. *(c & d)* Close-up illustrating the self-assembly of the monolayer at the water-air interface. *(e & f)* Stamping a lattice of larger polystyrene (PS) spheres onto the nanoparticle monolayer and peeling it away from the water droplet.

solution onto 25 mm^2 silicon chips and allowing them to dry. Our experiments used sphere diameters ranging from 100 nm to 1.9 μm. Because the nanoparticle monolayers readily adhere to the PS spheres, the layers delaminate from the water and transfer to the PS spheres, as when inking a stamp. These 'stamped' monolayers were then imaged using a Carl Zeiss Merlin scanning electron microscope (SEM).

MONOLAYER MORPHOLOGY: COVERAGE, CRACKS, AND FOLDS

SEM imaging revealed that the nanoparticle sheets reproducibly retain their monolayer structure as they are transferred onto the substrate of PS spheres. The sheet morphology, however, varies with the size of the PS spheres used. For PS diameters $D \approx 100$ nm, monolayers typically cover the substrate without cracks or folds (Fig. 2a). For these small D, the monolayers do not enter deeply into the crevices between spheres, instead getting pinned at the apex of each PS sphere and bridging the crevices as freestanding membranes.

Once D becomes larger, the stamped sheets are able to follow the substrate surface topography more closely, creating snugly fitting caps. Remarkably, the sheets conform tightly to the PS spheres up to polar angles (measured from the apex of each sphere) of 20-30° without buckling, wrinkling, or creating folds. This already indicates behavior quite distinct from that of other thin sheets, such as paper, mylar, polystyrene, or graphene, which invariably generate folds or rip [2, 16–19].

At larger polar angles, azimuthally oriented cracks appear, which hint at large radial stress as the sheets conform to the PS spheres during the stamping process. These cracks prevent the sheets from bridging the gap between neighboring spheres (Fig. 2b-c). For sphere diameters larger than roughly 1 μm, not only do the sheets tear azimuthally to form caps on each sphere, but also they form localized radial folds to accommodate the mismatch between flat and spherical metrics (Fig. 2d).

The azimuthal cracks in Fig. 2b-c and the radial folding lines in Fig. 2d form during the stamping process, in which the monolayers are deformed under vertical pressure to conform against the non-Gaussian topography, as sketched in Fig. 1. Once the nanoparticles are in contact with the polystyrene surface, the adhesion immobilizes these local deformations. For D around 200 nm, portions of the monolayer that did not adhere to PS spheres tend to tear in the interstices between polystyrene spheres. For larger D, the azimuthal fractures become more pronounced, allowing the interstitial portions of the sheet to recede further down (Fig. 2c). For the largest sphere sizes ($D \geq 690$ nm), the non-adhering portions may be swept away as the water dewets the chip while it is being pulled off the droplet at the end of the stamping process (Fig. 2d).

ENERGY SCALING

A simple geometric insight underpins the trend in behavior seen in Fig. 2. On a flat sheet, the circumference of a circle grows in proportion to its radius, r. On a sphere, however, the circumference of a circle at the same distance r from the sphere's apex grows more slowly due to the Gaussian curvature. In other words, when a flat disc of given r is made to conform to the surface of a sphere it must deform to compensate for the deficit in circumference. Elastic deformations can take the form of radial expansion, azimuthal compression, or some combination of the two.

If the sheets furthermore become pinned to the PS spheres during the stamping process, the nanoparticles attach sequentially one annulus at a time, starting from each sphere's apex (Fig. 4a). The amount of elastic deformation necessary to conform an annulus to the surface at

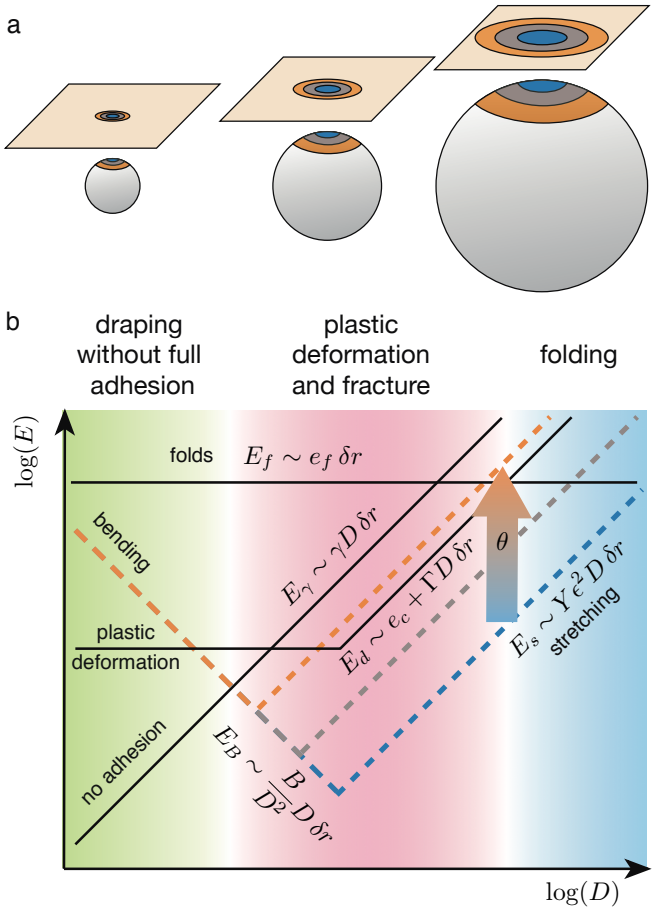

FIG. 4. **Energy scaling predicts changes in sheet morphology.** The interplay of different energy costs predicts crossovers from fully covered PS lattices (incomplete adhesion, green region), to plastic deformation (red region), to the formation of localized folds (blue region). Each energy is for a nanoparticle annulus of radial width δr — with stretching modulus Y and bending modulus B — and a PS sphere of diameter D. The energy cost of *not* adhering to the PS substrate, E_γ, grows with the area of the annulus, $\pi D \sin\theta\delta r$, as do the stretching energy, E_s (which also depends on the polar angle, θ, through the strain $\epsilon_{ij} = \epsilon_{ij}(\theta)$ as $E_s \sim D\sin\theta\delta r\theta^4$), and the energy of plastically deforming the annulus, E_d. E_d has a minimum set by the core energy of a dislocation. The energy of creating a localized fold, E_f, is set by the energy to crease the sheet. The fold energy per unit length of the fold, e_f, depends on the fold angle and microscopic details of the lattice.

a given polar angle, θ, increases with the size of the annulus and thus also with sphere diameter D. As successive annuli conform to the substrate, the cost of elastic energy may exceed the energetic costs associated with delaminating, forming defects, ripping apart, or folding. This is where a crossover to new stamped-sheet morphology occurs.

In the following, consider an annulus of nanoparticle sheet with radial width δr that has been conformed onto a PS sphere of diameter D to sit at polar angle θ. Such annulus has an area $\pi D\sin\theta\delta r$. Conforming this annulus to the sphere requires an areal bending energy density $\mathcal{E}_b \sim B/D^2$, where B is the sheet's 2D bending modulus, so that the total bending energy in the annulus becomes $E_b \sim (B/D)\sin\theta\delta r$ (here we are neglecting corrections of order $\mathcal{O}(\theta^2)$, see Supplementary Information). Thus, the cost of bending decreases as D grows. This contrasts with the fixed areal energy density $\mathcal{E}_\gamma$ relieved by adhering to the PS sphere. For the annulus, this translates into a total cost of *not* adhering to the substrate, $E_\gamma \sim D\sin\theta\delta r$, that increases linearly with D.

The total stretching energy, E_s, stored in the annulus is proportional to its surface area and the stretching energy density. This stretching energy density, $\mathcal{E}_s$, is a quartic function of polar angle on the sphere, $\mathcal{E}_s \sim \theta^4$. Therefore, the cost of stretching also increases linearly with D, but the magnitude depends sensitively on the polar angle: $E_s \sim D\sin\theta\delta r\,\theta^4$.

We pause momentarily to justify the quartic scaling of $\mathcal{E}_s \sim \theta^4$ on theoretical grounds. The integrated Gaussian curvature over a patch on a sphere scales as $2\pi\int_0^{R\theta_a} G\,r\,\mathrm{d}r \sim R^2\theta_a^2/R^2 = R^0\theta_a^2$, where θ_a is the maximum polar angle that has adhered to the sphere. The geometric frustration on the spherical cap is the source of elastic energy in an annulus of the sheet that has not yet conformed to the sphere. While the presence of a negative curvature kink at θ_a screens the stress far from the spherical cap ($r\to\infty$), the stress is continuous (and significant) at θ_a, so the effect of the kink can be neglected in determining the scaling of the energy density in the annulus that will next pin to the sphere. Just as the strain surrounding a wedge disclination of charge q embedded in a two dimensional material scales with its charge — that is, $\epsilon \sim q$ — so too the strain at θ_c scales with the integrated Gaussian curvature of the spherical cap: $\epsilon \sim \int_0^{R\theta_a} G\,r\,\mathrm{d}r \sim R^0\theta_a^2$. After annuli for a sequence of θ_a have adhered, we thus expect $\epsilon \sim \theta^2$. Linear elasticity gives $\sigma \sim Y\epsilon \sim \theta^2$ as well, and thus the stretching energy density $\mathcal{E}_s = \frac{1}{2}\sigma\epsilon \sim \theta^4$. The total stretching energy contained in a region of nanoparticle sheet up to θ_a would then scale as $E_s = 2\pi\int_0^{R\theta_a}\mathcal{E}_s r\mathrm{d}r \sim R^2\theta_a^6$. Sequential pinning of the nanoparticle sheet ensures that this is true irrespective of the maximum angle subtended by the sheet.

This analysis contrasts with the expectation for an equilibrated elastic sheet without pinning. Without pinning, the energy density rearranges in such a way as to be non-monotonic in the polar angle θ on the sphere, with some sensitivity to the boundary conditions. The stress is greatest on the apex of a sphere without pinning, in stark contrast to the case with sequential pinning, for which the stress vanishes at the cap. Solving for the unpinned situation exactly results in an integrated energy density which is roughly quadratic in polar angle: $E = 2\pi\int_0^r \mathcal{E}\,r\,\mathrm{d}r \sim R^2\theta^2$, with corrections of order

$\mathcal{O}(R^2\theta^4)$. This difference highlights the distinct character of sequential adhesion to a substrate seen in our system.

While the stretching energy scales as $E_s \sim D\sin\theta\delta r\,\theta^4$, the energy cost E_d of relieving stress through plastic deformation of the annulus scales similarly with sphere diameter, but has a sublinear scaling in θ: $E_d \sim max(E_{\rm disloc}, \Gamma D\sin\theta\delta r)$, where $E_{\rm disloc}$ is the energy of unbinding a single pair of dislocations and Γ is a phenomenological factor capturing the work required to damage a unit area of the material. The minimum possible energy to create the first defect, which corresponds to $E_{\rm disloc}$, sets the lower cutoff that freezes out defect proliferation at small D. $E_{\rm disloc}$ is determined by the core energy of a dislocation, e_c, as well as the elastic cost of deforming the portion of sheet surrounding the dislocations, which depends on microscopic features of the lattice. (We will return to $E_{\rm disloc}$ in a later section.) Finally, the energy cost for creating a fold in the sheet, E_f, increases only with the fold length ($\sim \delta r$) and thus is independent of D.

Fig. 4b represents these energy scaling relations schematically. Throughout this figure, linear and sublinear dependences on the polar angle θ are suppressed for clarity; while the adhesion energy scales with $\sin\theta$ and the bending energy experiences corrections of order $\mathcal{O}(\theta^2)$, we omit this dependence. However, we illustrate the strong θ dependence of the stretching energy by the colored dashed lines.

From this scaling we infer that for sufficiently small sphere sizes (or, equivalently, large Gaussian curvature), the lowest cost will be incurred by incomplete adhesion, as this causes the least distortion in the flat sheet. The green region in Fig. 4b represents this regime, which corresponds to the experimental results in Fig. 2a.

For larger sphere sizes, bending becomes energetically cheaper than not adhering. However, in order to conform tightly to the sphere, the monolayer needs to not only bend, but also stretch or compress. For annuli at small polar angles θ, this elastic energy cost can be negligible, but as θ grows for a given D, the cost will eventually exceed the penalty for creating defects. As a result, beyond some critical polar angle θ_c, plastic deformation in the sheet will cause a proliferation of dislocations. We expect that the formation of cracks follows as a result of this defect formation, along with the tension that remains while defects are formed. Since the in-plane stretching is tensile along the radial direction, cracks open up along the azimuth, perpendicular to the radial tension. This regime is represented by the red region in Fig. 4b and corresponds to the experimental results in Fig. 2b and c.

For the largest PS sphere sizes, yet another crossover occurs due to the difference in scaling between the costs for either elastic stretching or plastic deformation, which increase linearly in D, and the costs of forming localized folds, which is independent of D. This is the regime shown in blue in Fig. 4b, corresponding to Fig. 2d. Because the energy cost for fold formation lies below that of plastic deformation, the first response as strains build up will be to form folds rather than the proliferation of dislocations.

This energy scaling captures all three regimes of stamped nanoparticle sheet morphology seen in Fig. 2. We note that this framework operates in the continuum limit and assumes that linear elasticity holds in our system before the onset of plastic deformation. Nevertheless, the essential features are supported by quantitative comparisons with simulations given in the following section. Additionally, our picture assumes that chemical properties of the polystyrene do not vary with PS sphere size, an effect that could alter the adhesion energy in Fig. 4b.

In the remaining sections, we discuss in more detail each of the mechanical responses of the flat sheets to the enforced geometric mismatch: bending, stretching, dislocation proliferation, crack formation, and folding.

BENDING AND ADHESION

The crossover from incomplete adhesion to full adhesion with plastic deformation occurs in our experiments for PS spheres with diameters $D \approx 200$ nm. This crossover enables an estimate of the bending rigidity in nanoparticle membranes.

Near the apex of the sphere, the two-dimensional bending energy density of a thin plate in plane stress is [34]

$$\mathcal{F}_B \approx \frac{4B(\nu+1)}{D^2}, \tag{1}$$

as detailed in the Supplementary Information. We take the Poisson ratio to be $\nu = 1/3$, the value for a triangular lattice of spring-coupled nodes, in accordance with the measured value for nanoparticle sheets [21]. We take an average radius of curvature of $D/2 \approx 100$ nm for the crossover. Note that we expect a correction to the bending energy that scales quadratically with the polar angle, θ, which we neglect here (see Supplementary Information).

At the small-sphere crossover between incomplete adhesion and plastic behavior, we should expect the bending energy to match the adhesion of the nanoparticle sheet with polystyrene. Using the result of Ref. [22], we estimate the adhesion energy from the surface tensions of dodecane (21 mN/m) and water (72 mN/m), the surface energy of solid polystyrene ($\sim$ 42 mN/m) [23], and the molar volumes of each. The result is an adhesion energy of $\gamma_{\rm PS} + \gamma_{\rm dodecane} - \gamma_{\rm PS,dodecane} \approx 60$ mN/m. We expect that the bending energy, $\mathcal{F}_B$, matches this value at the crossover. This gives a bending modulus for the nanoparticle sheets of $B \approx 4.5 \times 10^{-16}$ Nm.

From this we may deduce a lower bound on the effective thickness t_{eff} of the sheets, which can deviate from the physical thickness of the sheet due to the non-continuum nature of the material [8]. The bending modulus is related to t_{eff} via $B = Yt_{\text{eff}}^2/12(1-\nu^2)$. Here the 2D stiffness $Y = Et$ is the product of Young's modulus E and physical thickness t. If we assume $E \sim 3$ GPa, as is appropriate for fully dried monolayers [5, 24], we obtain $t_{\text{eff}} \approx 14$ nm, about 60% larger than the physical thickness of $t \approx (d_{\text{Au NP}} + 2 \times \ell_{\text{ligand}})$ nm $= 8.2$ nm. However, we expect that during the stamping process there is residual water embedded in the ligand matrix. The presence of water molecules in the matrix has been shown to drastically affect the elastic properties, reducing elastic moduli by potentially several orders of magnitude [25, 26]. Such decrease in E then implies an increase in t_{eff}, possibly up to around $10t$ as observed for dried monolayers [8].

The crossover from incomplete adhesion on small spheres to tightly conforming to larger spheres is reminiscent of the crossover in a thin sheet's 'bendability', which is the ratio of tensile to bending forces, PR^2/B, where P is the tension at the edge of a sheet covering a PS sphere due to in-plane stretching or interfacial forces [14]. As the PS sphere size increases, so too does the bendability of the sheet. Our system differs from these recent studies of comparably stiff sheets, however, because of the strong pinning of the nanoparticle sheet to the substrate. The apparent force imbalance in the stretching of the sheet measured in simulations shows that adhesion enables a disproportionate increase in radial tension, at a rate faster than long-range elasticity would allow (Supplementary Information Fig. S3). Specifically, adhesion supplies a tension which offsets the imbalance of in-plane stresses, $\partial_r(r\sigma_{rr}) - \sigma_{\phi\phi}$. While this quantity would vanish without pinning, here the stress imbalance grows as θ^2 for small to moderate polar angles (see Supplementary Information).

STRAIN ANALYSIS

During the stamping process, the first contact between the nanoparticle sheet and a PS sphere occurs at the sphere's apex, $\theta = 0$, where the sheet will be pinned. Subsequent annuli of the sheet will need to strain or undergo plastic deformation in order to conform tightly to the surface of the PS sphere, but once this has occurred, these annuli also will become pinned to the polystyrene. This means that we can obtain information about the local strain by using the individual nanoparticles as markers and extracting differences in their average spacing along a sphere's surface. Given the random disorder inherent already in the flat sheets, this procedure requires ensemble averages over several different imaged PS spheres for statistically relevant results.

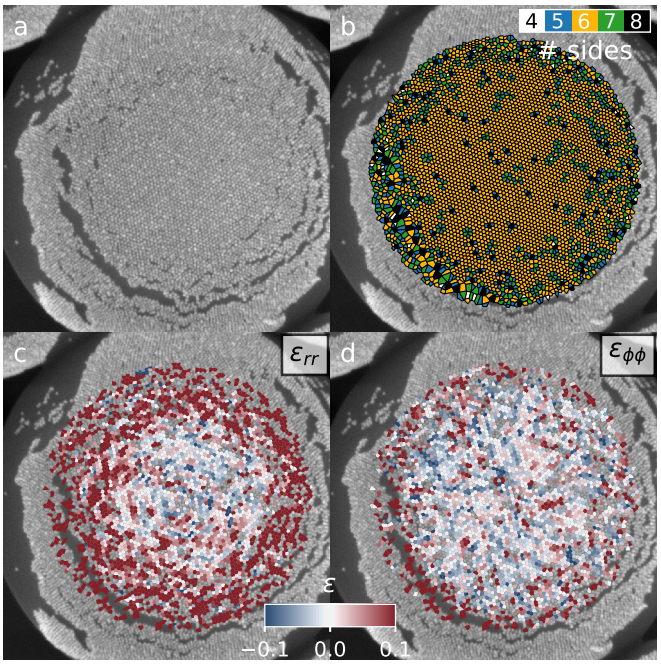

FIG. 5. **Identification of defects and extraction of the local strain tensor.** *(a)* Nanoparticles are identified in the original SEM image. *(b)* Using a Voronoi tessellation, we enumerate the neighbors of each nanoparticle. For each nanoparticle with six neighbors, comparing the Voronoi cell to a regular hexagon lying on the tangent plane of the sphere yields the strain tensor. To restrict the analysis to elastic deformations, we omit particles whose Voronoi cell is deformed well beyond the elastic limit of the material, keeping only hexagons whose perimeter to surface area ratio, $s \equiv P/\sqrt{A}$, satisfies $s < s_{\text{cutoff}} = 4.0$. *(c-d)* The radial strain in the sheet, ϵ_{rr}, increases with distance from the apex, while azimuthal strain, $\epsilon_{\phi\phi}$, does not.

Image analysis

To study the strains and defect densities of nanoparticle sheets, we use a custom image analysis routine on each SEM image to identify the nanoparticle locations and to identify the nearest-neighbor connectivity of the nanoparticle lattice [27]. We bandpass each image in two steps: first convolving it with a Gaussian (whose parameters include nanoparticle characteristics such as lattice spacing) and then convolving the result with a boxcar function. Subtracting the two gives a high-pass-filtered image from which we extract particle positions.

A Delaunay triangulation provides the lattice topology and the nearest neighbors for each particle. Defects in the lattice are particles with fewer than six or greater than six neighbors (disclinations), and pairs of oppositely signed disclinations form dislocations (for example, a 5-7 disclination pair). Fig. 5b shows an example Voronoi tesselation of a triangulated nanoparticle sheet draped on a 690 nm diameter PS sphere. The Delaunay triangulation also enables a direct measurement of the local

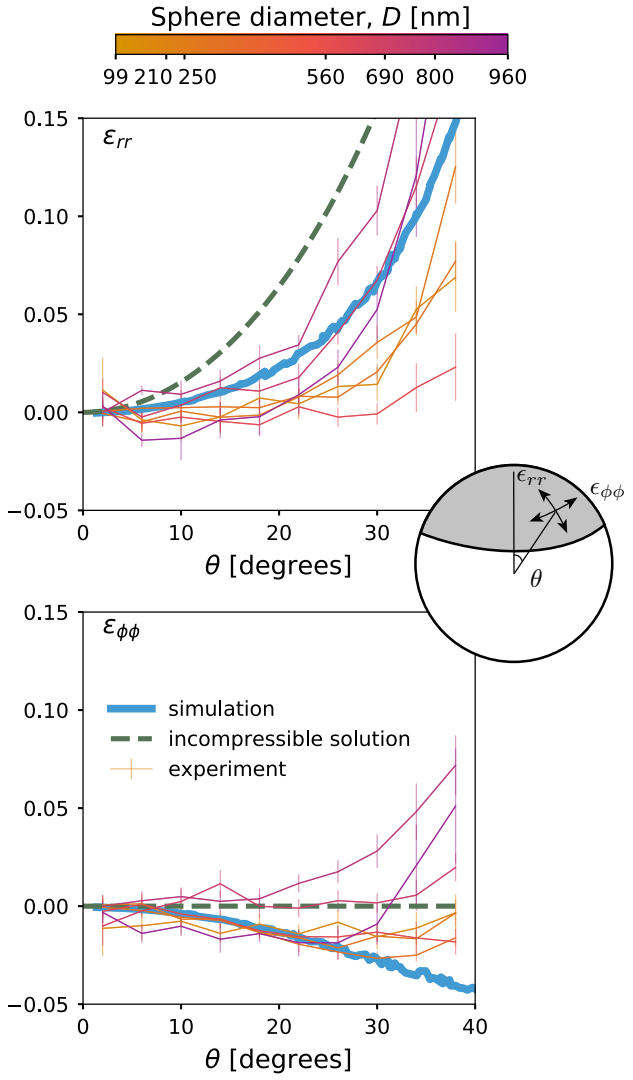

FIG. 6. **Strain analysis shows qualitative agreement between experiments and simulations.** Data from nanoparticle sheets on 62 imaged PS spheres of different diameters reveals that the radial strain, ϵ_{rr} increases with polar angle, while the azimuthal strain, $\epsilon_{\phi\phi}$, is compressive and comparatively small.

strain tensor, ϵ_{ij}. For particles with exactly six neighbors, we measure the displacements of its neighbors from a regular hexagon with bonds of unit length. In this step, we account for the non-planar geometry of the substrate by computing displacements only in the tangent plane to the underlying PS sphere. By comparing each triad of the central particle and two adjacent neighbors to an undeformed reference triangle, we obtain a strain tensor for that triad of nanoparticles. For each particle that is not a defect, the average strain field of its six shared triangles represents a measure of local strain. This strain measurement is well-defined only for particles that have six nearest neighbors — that is, those particles which do

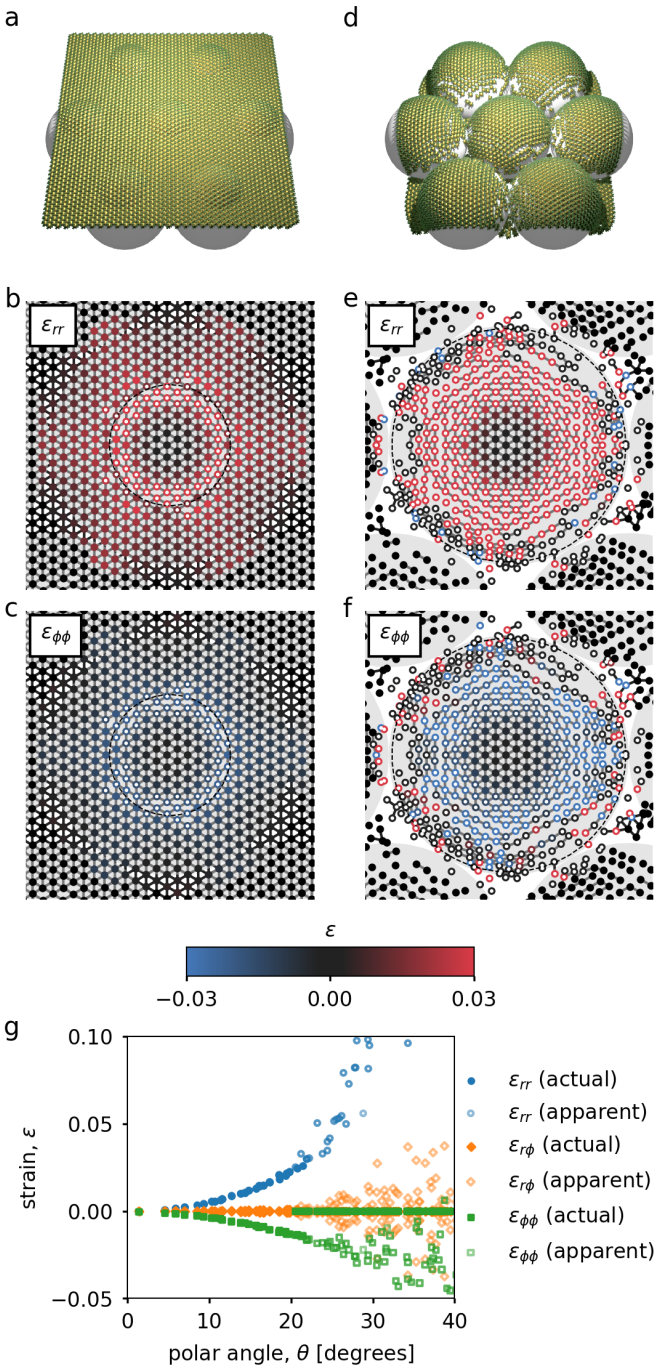

FIG. 7. **Simulations of spring networks.** Spring networks were made to conform to a lattice of spheres, as in Fig. 1. Bonds with $\geq 3\%$ strain are removed at each time step, mimicking bond breakage. *(a-c)* As a flat, triangular spring network is pressed against an array of spheres, each node is immobilized upon contact with a substrate sphere. As the network conforms, strains build up, leading to bond breaking for polar angles larger than $\theta \sim 23^\circ$. Particles with severed bonds are colored white at their centers in the strain images. *(d-f)* Layers of bonds continue to adhere to the substrate with many radial bonds broken. *(g)* Though the actual strains in the network's springs do not exceed 3%, the apparent strain inferred from the placement of nanoparticles continues to increase in the damaged annuli.

not form topological defects in the lattice.

Identifying the center of the PS substrate spheres by fitting their profile to a circle, we rotate the strain field ϵ_{ij} into polar coordinates $(\epsilon_{rr}, \epsilon_{r\phi}, \epsilon_{\phi\phi})$ and average annular bins (i.e., bins of $\phi_i < \phi < \phi_{i+1}$) to obtain curves for $\epsilon_{rr}(\theta)$ and $\epsilon_{\phi\phi}(\theta)$ as a function of polar angle on a sphere. Typical results are shown in Fig. 5c-d. Fig. 6 shows strain curves averaged over several spheres and images for each sphere size. To further reduce noise from voids and defects, we also omit particles whose Voronoi cells are deformed well beyond the elastic limit of the material. Specifically, we enforce a cutoff in the shape parameter s, defined as the ratio of the perimeter of the hexagon to the square root of its surface area, $s \equiv P/\sqrt{A}$. Here, we use the cutoff $s < s_{\text{cutoff}} = 4.0$. The results are not significantly sensitive to the value of this cutoff, so long as $s_{\text{cutoff}} \gtrsim 3.9$.

Fig. 6 shows the average strain tensor components as a function of polar angle for different sphere sizes. The analysis indicates that the sheet's radial tension grows substantially, while the strain along the azimuth of the PS sphere is weakly compressive. The shear strain averages to zero, as predicted by the symmetry of the spherical geometry, with variations in the measured mean shear of $< 1\%$. As mentioned above, the nanoparticle sheets' inherent disorder creates a distribution of strain component values for each binned annulus. These distributions have a standard deviation of $\sim 10\%$ strain — significantly larger than the strains themselves for all but the largest values of θ considered. By averaging the strains in annular bins on each PS sphere and by performing ensemble averages over different spheres, the disorder on the scale of individual nanoparticles is largely averaged out. As Fig. 6 shows, these ensemble-averaged data can show quantitative (and in some cases for the azimuthal strain also qualitative) differences as the PS sphere diameter D is varied. This likely is due to slight, unavoidable variations in the sample preparation conditions. However, within this variability we find no clearly discernible trends as a function of D. Considered in aggregate, these data can therefore be used for qualitative comparison with models, as we discuss next.

Spring network simulations

To gain insight into the elastic behavior during the stamping process, we model the nanoparticle sheet as a flat, triangular spring network. Simulations of such networks pinned to a lattice of spheres reproduce the trends in strain observed in the experiments (Fig. 6 and Supplementary Videos 1-3).

The simulations proceed by minimizing the free energy of a triangular spring network at each time step using a conjugate gradient method as we deposit the network onto a lattice of spheres. Whenever a node of the spring network made contact with a substrate sphere, we irreversibly pinned that node to the point of contact for the remainder of the simulation. Increasing the radii of the substrate spheres with respect to the bond length by a factor of two (and, proportionately, scaling the number of nanoparticles by a factor of four) gave virtually identical results for the strain plots given in Fig. 6 and Fig. 7, indicating that the simulations are representative of the continuum limit. Study of the finite size scaling shows that the strain curves deviate significantly from the continuum limit only for substrate sphere sizes below $D \lesssim 10a$, where a is the lattice spacing (see Supplementary Information Fig. S5).

In the simulations, a sheet began at a distance $R = D/2$ above the plane containing the centers of the substrate spheres, each of diameter D. The network was then lowered in small increments $(0.001D)$ and the free energy was minimized for that configuration, subject to the constraint that all particles (nodes of the spring network) must lie in the common membrane plane or on a sphere, whichever is higher in the z dimension. For each step, a sequence of random kicks were applied to each node to escape local minima in the energy landscape. At the end of the relaxation process, nodes in contact with a substrate sphere — that is, within a small threshold of $10^{-5}a$, where a is the rest bond length (lattice spacing) — are marked as immobilized for the remainder of the simulation.

As shown by the blue curves in Fig. 6, as well as in Supplementary Videos 1 and 2, these simulations of perfectly elastic triangular networks show similar behavior in both ϵ_{rr} and $\epsilon_{\phi\phi}$ as a function of polar angle on the underlying sphere. As the membrane begins to conform to the sphere lattice, pinning ensures that the apex of the sphere experiences negligible strain, as expected. The radial stress increases quadratically, while a compressive azimuthal stress builds up more slowly. The deviation of $\epsilon_{\phi\phi}$ between experiment and simulation at large θ is due in part to the failure and plastic deformation of the actual sheets, which is suppressed in the simulations we show in Fig. 6 (see also Supplementary Video 3).

Comparison with incompressible solution

Considering the limit in which the nanoparticle sheet is incompressible allows for a useful point of reference against which we can compare the iterative adhesion of nanoparticle annuli. The strains required to conform to the substrate in this limit are indicated by the green dashed line in Fig. 6. Namely,

$$\epsilon_{rr} = \sqrt{\frac{R^2}{(R^2 - r^2)}} - 1, \tag{2}$$

where $R = D/2$ is the radius of the PS sphere, while $\epsilon_{\phi\phi} = 0$ due to incompressibility. All data, whether experimental or simulation-based, lie below this solution for ϵ_{rr}. This clearly indicates compressible behavior of our nanoparticle sheets.

The material cannot stretch elastically without bound: sufficiently large strains will plastically deform the sheet, severing bonds between nanoparticles to form cracks or dislocations. Indeed, the radial strains seen in Fig. 6 greatly exceed the critical strain for failure in flat nanoparticle membranes [15]. While we will consider plastic deformation in the next section, we note that introducing failure into the spring network simulations generates qualitatively similar morphologies to those seen in experiment. Fig. 7 demonstrates that introducing a nominal breaking strain of 3% leads to the formation of partially intact annuli separated by azimuthal cracks. In panel *c* of Fig. 7, we show both the strains of particles with all original bonds intact (closed markers) as well as the 'apparent' strain (open markers) resulting from triangulating the point pattern and including all particles with six nearest neighbors, regardless of whether the bonds connecting them have severed. This gives strains that remain qualitatively similar to those seen in experiment, with increased scatter in the apparent strains frozen into the broken regions pinned to the substrate.

PLASTIC DEFORMATION

Given that a flat nanoparticle lattice forms a close-packed array of hexagons, any particles who do not have six nearest neighbors are defects. We record the location of each defective particle and its number of nearest neighbors. Fig. 5b shows the Voronoi tessellation of one representative lattice overlaying the original SEM image. Each yellow site corresponds to a nanoparticle having six nearest neighbors (i.e., a hexagon), while defects are colored white, blue, green, and black for coordination numbers of $z = 4, 5, 7$, and 8, respectively.

As the sheet begins to respond with plastic deformation, dislocations proliferate in the material. The density of dislocations correspondingly increases with polar angle on a sphere, as can be seen in Fig. 5b. We observe that azimuthal cracks form only beyond the point of dislocation proliferation, which suggests that the material yields plastically before cracks coalesce.

Formation of dislocations

The scaling arguments presented in Fig. 4 predict that plastic deformation should be favorable at a critical angle independent of sphere diameter D. Nevertheless, in our experiments, we observe an increase in the polar angle at which dislocations appear for the smallest PS sphere sizes, shown in Fig. 8.

As expected, the by far most prominent types of strain-induced defects in the nanoparticle arrangement are dislocations — i.e., pairs of Voronoi cells with 5 and 7 sides. Fig. 8a shows a representative measurement of the crossover from low to high defect density as a function of polar angle, θ. These data were obtained from ensemble averages over Voronoi tessellations such as that shown in Fig. 5b. For each PS sphere diameter D, we identify a characteristic angle at which the number of defects begins to grow significantly (black dashed line in Fig. 8a). This analysis leads to the black data in Fig. 8b, which shows the characteristic angle as a function of D. This angle approaches a constant value consistent with scale-invariance in the continuum limit of large PS sphere sizes, where the nanoparticle lattice spacing becomes irrelevant. However, we observe an increase in the angle for the smallest PS sphere sizes. This observed variation in the onset of dislocation proliferation suggests that the discrete nature of the lattice becomes important for small D.

If we approximate our sheet as a locally flat, two-dimensional lattice, each dislocation pair costs an elastic energy [28]

$$E_{\text{disloc}} \approx \frac{\mu a^2}{2\pi(1-\nu)} \ln\left(\frac{\ell}{a}\right), \tag{3}$$

where Y is the sheet stiffness, ν is the Poisson ratio, ℓ is the final distance between the unbound dislocations, and a is the lattice spacing. We assume the elastic core energy, e_c, to be small compared to the elastic energy in the deformed sheet, with the understanding that Equation 3 represents a lower bound. Below, we consider $\ell \approx 1/3\sqrt{\rho}$, as illustrated in the inset of Fig. 8. Here, ρ is the density of dislocations (so that ρ^{-1} approximates the area of a patch whose elastic deformation is dominated by the dislocation's presence). Note that we expect this elastic energy to be felt predominantly in regions of the material which are not already pinned to the underlying substrate.

In order to find a lower bound for the critical angle at which defects may appear, we compare the dislocation unbinding energy (Equation 3) with the stretching energy for the sheet to conform to a sphere. Using the results from spring network simulations, we equate the stretching energy available in an annulus of width chosen to be $\delta r = a$ with the unbinding energy of Equation 3. This gives the blue solid line in Fig. 8 for $\ell = (3\sqrt{\rho})^{-1}$, with the blue band denoting the range of results given the standard deviation of measurements for ρ across sheets on all PS spheres included in the analysis. As seen by the width of the blue band, the prediction is moderately sensitive to the assumed distance that the unbound dislocation travel apart in their creation. We measured the dislocation density, ρ, from the relative frequency of dislocations at $\theta = 0$ in experiments. Despite the approxi-

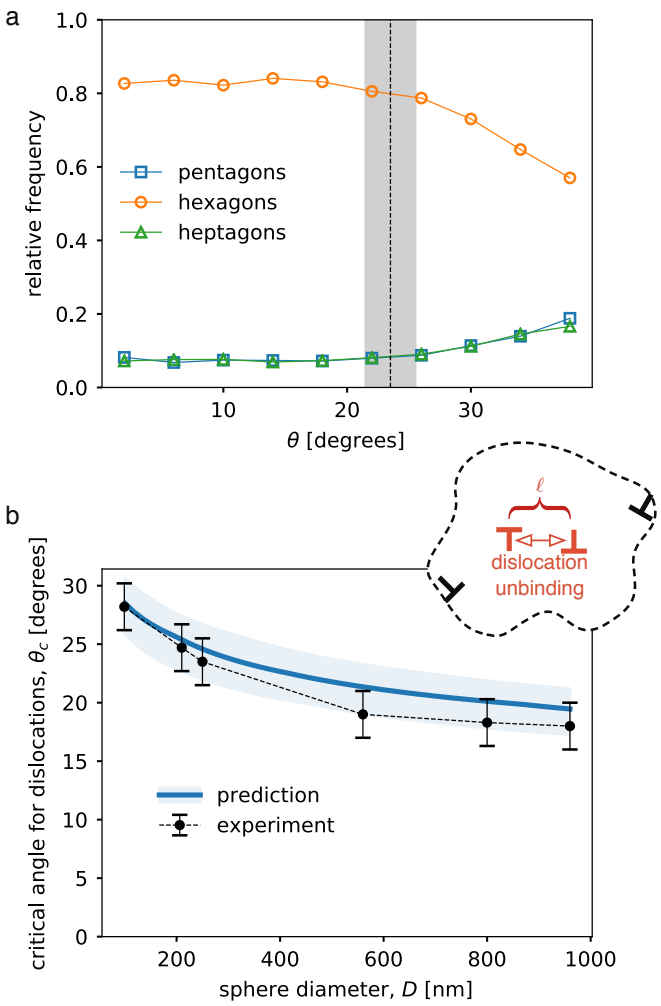

FIG. 8. **Strain-induced defects in the nanoparticle sheets.** *(a)* The proliferation of defects results in increasing dislocation frequency (and correspondingly, to a decreasing frequency of hexagons) as a function of polar angle, θ. An example of the angle-dependence of defect densities is shown for nanoparticle sheets conformed to 250 nm PS spheres. Here, a crossover appears near $\theta_c \sim 24°$. *(b)* For small sphere diameters, the characteristic angle for defect proliferation deviates from its continuum value, with smaller PS spheres triggering the formation of defects at larger polar angles. An idealized prediction for the energy of a single defect provides a rough estimate for the critical angle (blue curve with blue band denoting the uncertainty from the spread in measurements of the defect density). Data for the smallest sphere diameters included only sheets stamped on isolated spheres, not sheets which cover close-packed PS lattices.

mate nature of the derivation, the prediction lies within our experimental uncertainty for changes in the choice of δr by up to a factor of three, and the agreement in the shape of $\theta_c(D)$ is notable.

Formation of azimuthal cracks

Another response to the buildup of strain is to form cracks in a material. This irreversible deformation relieves elastic energy by severing bonds between nanoparticles. We find that, for PS sphere sizes above 210 nm, nanoparticle sheets generally form azimuthal cracks such as those seen in Fig. 2c and Fig. 5.

From a geometric standpoint, projecting an annular strip of inner diameter $R\theta_0$ from a flat disk onto a sphere of radius R involves less azimuthal compression if the annulus is placed at a polar angle $\theta_1 > \theta_0$. This fact is reflected in our experiments and simulations, with radial strain building up with increasing polar angle. Once the radial strains are sufficient to rip apart bonds to form azimuthal cracks, we expect that as the next portion of the membrane drapes onto the sphere, it is energetically favorable to adhere to a location further down, where $\theta_1 > \theta_0$. The result is a portion of uncovered PS sphere between θ_0 and θ_1, i.e., an azimuthal crack imprinted on the spherical substrate.

FORMATION OF FOLDS AT LARGE SPHERE SIZES

For the largest PS sphere sizes, the caps formed by the adhering nanoparticle sheets are large enough that radially oriented folds can be observed (Fig. 2d). Such folds provide an alternate mechanism to map circles in the plane to circles on a sphere while minimizing radial tension and azimuthal compression. Localizing elastic energy into folds relieves the stretching in intervening patches, but because of the very high curvature at the fold, which we expect to be comparable to the inverse lattice constant, $\kappa \sim a^{-1}$, the energetic barrier to fold formation is larger than the bending energy by a factor $\sim D^2/a^2$. Yet, the large cost of having a fold in an annulus of fixed width, δr, does not scale with sphere diameter D, so that fold formation is no longer frozen out for large D, where the elastic cost of stretching grows higher and higher (Fig. 4).

In previous studies of folding that subjected thin sheets to uniaxial compression or out-of-plane deformation, folds typically spanned the whole system [29–31]. Here, however, the folds terminate within the sheet. As seen in Fig. 2, the fold terminus occurs at another characteristic polar angle, and the amount of material stored in each fold grows further from the apex of the sphere in order to accommodate the curvature of the underlying substrate. This type of fold also appears in skirts and other clothing, where it is called a 'dart'. While we robustly observe pronounced folds on large PS spheres, we find no evidence for smaller-scale wrinkling in the sheets. This can be predicted from the energy scaling (Fig. 4): the cost to delaminate from the PS surface exceeds both

folding and stretching energies ($E_\gamma > E_f, E_s$).

CONCLUSIONS

In this article, we focused on the ability of preassembled nanoparticle monolayer sheets to conform to a substrate composed of a lattice of larger spheres. With its local Gaussian curvature, κ, which can be tuned by varying the sphere diameter, such a substrate serves as a model for arbitrary surface topographies. In the presence of strong pinning to the substrate, the area mismatch between flat ($\kappa = 0$) and spherical ($\kappa > 0$) geometries triggers a competition between different deformation modes of the sheet, including delamination, bending, stretching, fracture, and folding.

Treating the sheets as homogeneous continuum material correctly predicts many aspects of the elastic deformation. For comparison with experiments, the local strain tensor components were extracted from a statistical analysis of images of the sheets, where the nanoparticles served as distance markers. On the other hand, the details of plastic deformation are only captured if the discrete nature of the sheets is taken into account, which enables changes in the number of nearest neighbors for individual particles. By tracking the onset of strain-induced dislocations within the sheets, we are able to explain deviations from the continuum predictions, which are found when the sheets are conformed to substrates with small D, corresponding to regions of large κ.

The observed morphologies for the stamped sheets highlight the remarkable ability of nanoparticle monolayers to cope with strain through a combination of elastic and plastic deformations. This material contrasts with other thin sheets such as paper, mylar, or graphene, which lack a similar mechanism for generating particle dislocations.

There is currently much interest in creating functional materials by stacking ultrathin, essentially 2D layers with different electronic or optical properties [32, 33]. So far, such stacking has been limited to flat substrates, where it is relatively easy to obtain good interfaces between successively deposited layers. In this regard, the ability of nanoparticle sheets to comply and conform opens up new possibilities for creating stacked layers with well-controlled interfaces also on more complex substrate topographies.

ACKNOWLEDGEMENTS

We thank Anton Souslov, Vincenzo Vitelli, and William Irvine for useful discussions. This work was supported by the Office of Naval Research under award ONR-N00014-17-1-2342 and by the National Science Foundation under award DMR-1508110. Additional support was provided by the University of Chicago Materials Research Science and Engineering Center, which is funded by National Science Foundation under award number DMR-1420709. Use of the Center for Nanoscale Materials was supported by the U.S. Department of Energy, Office of Science, Office of Basic Energy Sciences, under Contract No. DE-AC02-06CH11357.

* npmitchell@uchicago.edu; Corresponding author; Equal contribution
† Equal contribution
‡ jaeger@uchicago.edu; Corresponding author

[1] N. P. Mitchell, V. Koning, V. Vitelli, and W. T. M. Irvine, Nat Mater **16**, 89 (2017).
[2] J. Hure, B. Roman, and J. Bico, Phys. Rev. Lett. **106**, 174301 (2011).
[3] Z. Nie, A. Petukhova, and E. Kumacheva, Nature Nanotechnology **5**, 15 (2010).
[4] A. Dong, J. Chen, P. M. Vora, J. M. Kikkawa, and C. B. Murray, Nature **466**, 474 (2010).
[5] K. E. Mueggenburg, X.-M. Lin, R. H. Goldsmith, and H. M. Jaeger, Nat Mater **6**, 656 (2007).
[6] X. W. Gu, X. Ye, D. M. Koshy, S. Vachhani, P. Hosemann, and A. P. Alivisatos, PNAS **114**, 2836 (2017).
[7] K. M. Salerno, D. S. Bolintineanu, J. M. D. Lane, and G. S. Grest, Phys. Rev. Lett. **113**, 258301 (2014).
[8] Y. Wang, J. Liao, S. P. McBride, E. Efrati, X.-M. Lin, and H. M. Jaeger, Nano Lett. **15**, 6732 (2015).
[9] S. M. Rupich, F. C. Castro, W. T. M. Irvine, and D. V. Talapin, Nat Commun **5**, 5045 (2014).
[10] W. T. M. Irvine, V. Vitelli, and P. M. Chaikin, Nature **468**, 947 (2010).
[11] R. E. Guerra, C. P. Kelleher, A. D. Hollingsworth, and P. M. Chaikin, Nature **554**, 346 (2018), arXiv: 1802.04341.
[12] G. Meng, J. Paulose, D. R. Nelson, and V. N. Manoharan, Science **343**, 634 (2014).
[13] J. D. Paulsen, V. Dmery, K. B. Toga, Z. Qiu, T. P. Russell, B. Davidovitch, and N. Menon, Phys. Rev. Lett. **118**, 048004 (2017).
[14] H. King, R. D. Schroll, B. Davidovitch, and N. Menon, PNAS **109**, 9716 (2012).
[15] Y. Wang, P. Kanjanaboos, E. Barry, S. Mcbride, X.-M. Lin, and H. M. Jaeger, Nano Lett. **14**, 826 (2014).
[16] J. Hure, B. Roman, and J. Bico, Phys. Rev. Lett. **109**, 054302 (2012).
[17] J. D. Paulsen, V. Dmery, C. D. Santangelo, T. P. Russell, B. Davidovitch, and N. Menon, Nature Materials **14**, 1206 (2015).
[18] C. Lee, X. Wei, J. W. Kysar, and J. Hone, Science **321**, 385 (2008).
[19] L. H. Dudte, E. Vouga, T. Tachi, and L. Mahadevan, Nature Materials **15**, 583 (2016).
[34] L. D. Landau and E. M. Lifshitz, in *Theory of Elasticity (Third Edition)* (Butterworth-Heinemann, Oxford, 1986) pp. 38–86.
[21] P. Kanjanaboos, A. Joshi-Imre, X.-M. Lin, and H. M. Jaeger, Nano Lett. **11**, 2567 (2011).

[22] L. A. Girifalco and R. J. Good, J. Phys. Chem. **61**, 904 (1957).
[23] S. Wu, Journal of Polymer Science Part C: Polymer Symposia **34**, 19 (2007).
[24] J. He, P. Kanjanaboos, N. L. Frazer, A. Weis, X.-M. Lin, and H. M. Jaeger, Small **6**, 1449 (2010).
[25] Y. Wang, H. Chan, B. Narayanan, S. P. McBride, S. K. R. S. Sankaranarayanan, X.-M. Lin, and H. M. Jaeger, ACS Nano **11**, 8026 (2017).
[26] S. D. Griesemer, S. S. You, P. Kanjanaboos, M. Calabro, H. M. Jaeger, S. A. Rice, and B. Lin, Soft Matter **13**, 3125 (2017).
[27] J. C. Crocker and D. G. Grier, Journal of Colloid and Interface Science **179**, 298 (1996).
[28] J. Weertman and J. Weertman, *Elementary Dislocation Theory* (Oxford University Press, Oxford, New York, 1992).
[29] L. Pocivavsek, R. Dellsy, A. Kern, S. Johnson, B. Lin, K. Y. C. Lee, and E. Cerda, Science **320**, 912 (2008).
[30] D. P. Holmes and A. J. Crosby, Phys. Rev. Lett. **105**, 038303 (2010).
[31] P. Kim, M. Abkarian, and H. A. Stone, Nature Materials **10**, 952 (2011).
[32] C. Androulidakis, K. Zhang, M. Robertson, and S. Tawfick, 2D Mater. **5**, 032005 (2018).
[33] K. Kang, K.-H. Lee, Y. Han, H. Gao, S. Xie, D. A. Muller, and J. Park, Nature **550**, 229 (2017).
[34] L. D. Landau and E. M. Lifshitz, in *Theory of Elasticity (Third Edition)* (Butterworth-Heinemann, Oxford, 1986) pp. 38–86.

Supplementary Information for 'Conforming nanoparticle sheets to surfaces with Gaussian curvature'

BENDING

In Figure 4 of the main text, we omit linear and sub-linear dependences on the polar angle, θ, for clarity. As a result, the bending energies for different polar angles (blue, gray, and orange dashed lines) are shown to lie atop each other. Here we note that, in fact, we expect some dependence on polar angle, though this should appear as a subleading, quadratic correction to the bending energy on the apex of a PS sphere.

The two-dimensional bending energy density of a thin plate in plane stress is [34]

$$\mathcal{F}_B = \frac{B}{2}\left[\left(\nabla^2\zeta\right)^2 + 2(1-\nu)\left\{\left(\frac{\partial^2\zeta}{\partial x\partial y}\right)^2 - \frac{\partial^2\zeta}{\partial x^2}\frac{\partial^2\zeta}{\partial y^2}\right\}\right], \quad \text{(S1)}$$

where $\zeta(x,y)$ is the out-of-plane displacement of the plate and B is the bending modulus. Taylor expanding around $\theta = 0$, the energy density evaluates to

$$\mathcal{F}_B = \frac{B}{R^2}\left[(\nu+1) + 2(\nu+1)\theta^2 + \frac{14\nu+17}{6}\theta^4 + \mathcal{O}\left(\theta^5\right)\right]. \quad \text{(S2)}$$

Thus, we expect the bending energy of a membrane to increase with polar angle. This analysis neglects the presence of neighboring spheres, which would further affect the θ dependence, particularly at large θ, where the small deflection assumption and the validity of Equation S2 breaks down.

STRETCHING

Assuming locally in-plane displacements $\mathbf{u}(r,\phi) = u_r(r,\phi)\hat{\mathbf{r}} + u_\phi(r,\phi)\hat{\boldsymbol{\phi}}$, we have strains [34]

$$\epsilon_{rr} = \partial_r u_r \quad \text{(S3)}$$

$$\epsilon_{\phi\phi} = \frac{1}{r}\partial_\phi u_\phi + \frac{1}{r}u_r \quad \text{(S4)}$$

$$\epsilon_{r\phi} = \frac{1}{2}\left(\frac{1}{r}\partial_\phi u_r + \partial_r u_\phi\right). \quad \text{(S5)}$$

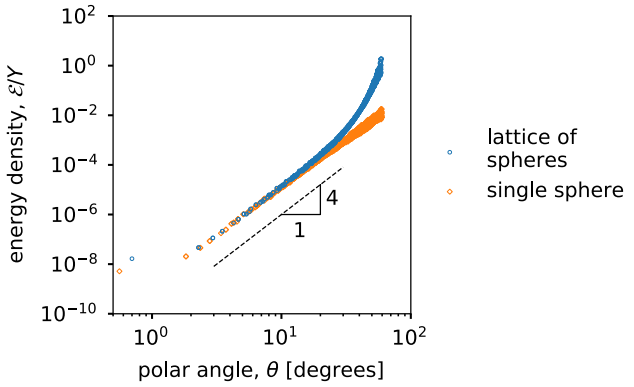

FIG. S1. **Stretching energy in a spring network draped on a lattice of spheres with strong pinning.** The energy density in a pinned sheet draped to a lattice of spheres grows as θ^4. Only at moderately large polar angles ($\theta \gtrsim 25^\circ$) does the stretching energy in a sheet conforming to a triangular lattice of spheres (blue circles) diverge from the case of a single sphere (orange diamonds). The quartic scaling with polar angle is exact in the absence of neighboring substrate spheres (orange diamonds). Both spring networks were $100\,a \times 100\,a$ in extent, and the substrate sphere diameters were $40\,a$ and $60\,a$ for the lattice and single sphere cases, respectively.

When the out-of-plane displacements are included, the expressions for strain become

$$\epsilon_{rr} = \partial_r u_r + \frac{1}{2}(\partial_r\zeta)^2 \quad \text{(S6)}$$

$$\epsilon_{\phi\phi} = \frac{1}{r}\partial_\phi u_\phi + \frac{1}{r}u_r + \frac{1}{2r^2}(\partial_\phi\zeta)^2 \quad \text{(S7)}$$

$$\epsilon_{r\phi} = \frac{1}{2}\left(\frac{1}{r}\partial_\phi u_r + \partial_r u_\phi + \frac{1}{r}\partial_r\zeta\partial_\phi\zeta\right). \quad \text{(S8)}$$

These strains are related to the stress via

$$\sigma_{rr} = \frac{Y}{1-\nu^2}(\epsilon_{rr} + \nu\epsilon_{\phi\phi}) \quad \text{(S9)}$$

$$\sigma_{\phi\phi} = \frac{Y}{1-\nu^2}(\epsilon_{\phi\phi} + \nu\epsilon_{rr}) \quad \text{(S10)}$$

$$\sigma_{r\phi} = \frac{Y}{1+\nu}\epsilon_{r\phi}, \quad \text{(S11)}$$

where $Y = Et$ is the stiffness.

The local energy density, $E_s = \frac{1}{2}\sigma_{ij}\epsilon_{ij}$, takes the plane stress form

$$E_s = \frac{Y}{1-\nu^2}\left(\frac{\epsilon_{rr}^2 + \epsilon_{\phi\phi}^2}{2} + \nu\epsilon_{rr}\epsilon_{\phi\phi}\right) + \frac{2Y}{1+\nu}\epsilon_{r\phi}^2. \quad \text{(S12)}$$

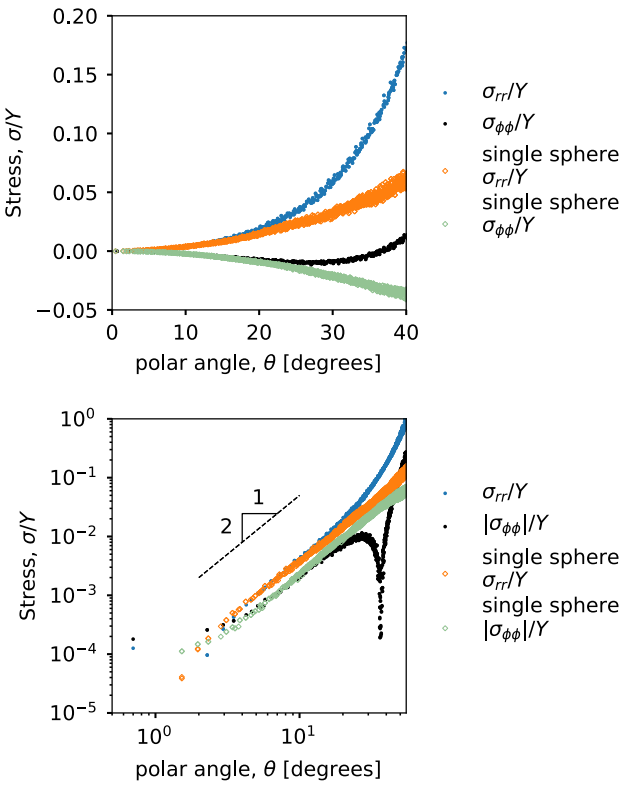

FIG. S2. **In-plane stresses in a spring network draped on a lattice of spheres with strong pinning.** The stress density in a pinned sheet draped to a lattice of spheres grows as θ^2. Only at moderately large polar angles ($\theta \gtrsim 25°$) does the stretching energy in a sheet conforming to a triangular lattice of spheres (blue circles) diverge from the case of a single sphere (orange diamonds). The quadratic scaling with polar angle is exact in the absence of neighboring substrate spheres (gray and orange diamonds for σ_{rr} and $\sigma_{\phi\phi}$, respectively.) The lattice dimensions are the same as in Fig. S1.

For shear-free strain configurations on the sphere,

$$E_s = \frac{Y}{1-\nu^2}\left(\frac{\epsilon_{rr}^2 + \epsilon_{\phi\phi}^2}{2} + \nu\epsilon_{rr}\epsilon_{\phi\phi}\right). \tag{S13}$$

Fig. S1 shows the stretching energy of an elastic spring network as a function of polar angle on the sphere. We find the stretching energy density grows as $\sim \theta^4$ for modest polar angle. Additionally, each component of the stress also exhibits clean scaling when only a single sphere is present as the substrate, as shown in Fig. S2. The presence of neighboring spheres in the substrate causes deviation from the power-law scaling in both energy density and stress for sufficiently large polar angles ($\theta \sim 20$ degrees).

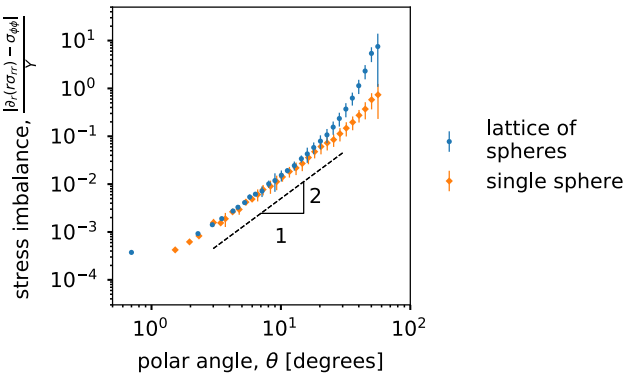

FIG. S3. **Adhesion enables an in-plane stress imbalance to the elastic membrane.** Through adhesion to the substrate, there is a residual force imbalance in the stretching of a simulated triangular spring network. The quadratic scaling with polar angle is exact in the absence of neighboring substrate spheres (orange diamonds). Both spring networks were $100\,a \times 100\,a$ in extent, and the substrate sphere diameters were $40\,a$ and $60\,a$ for the lattice and single sphere cases, respectively.

Influence of adhesion

Fig. S3 shows that for modest polar angles, the in-plane stress imbalance

$$\mathcal{I} \equiv \partial_r(r\sigma_{rr}) - \sigma_{\phi\phi} \tag{S14}$$

grows quadratically in simulations of spring networks draping to spheres. Without adhesion, this quantity would vanish in equilibrium. We checked that the residual force imbalance is scale-independent for sufficiently large substrate sphere sizes ($D/a \gtrsim 10$).

If adhesion is not included, then the resulting strain field constrasts with the results from simulations, as shown in Fig. S4. The strain field can be computed for this case without adhesion to the substrate sphere by solving for the Airy stress function, χ, which is sourced by the Gaussian curvature of the substrate:

$$\frac{1}{Y}\nabla^4\chi = -G = -\frac{4}{D^2}. \tag{S15}$$

The strain fields are then

$$\epsilon_{rr} = \frac{1}{4D^2}\left[(3\nu-1)\theta^2 - (\nu-1)W^2\right] \tag{S16}$$

$$\epsilon_{\phi\phi} = \frac{1}{4D^2}\left[(\nu-3)\theta^2 - (\nu-1)W^2\right], \tag{S17}$$

where W is the width of the sheet. The qualitative differences in elastic response shown in Fig. S4 highlight the importance of adhesion in determining the mechanical response and monolayer morphology.

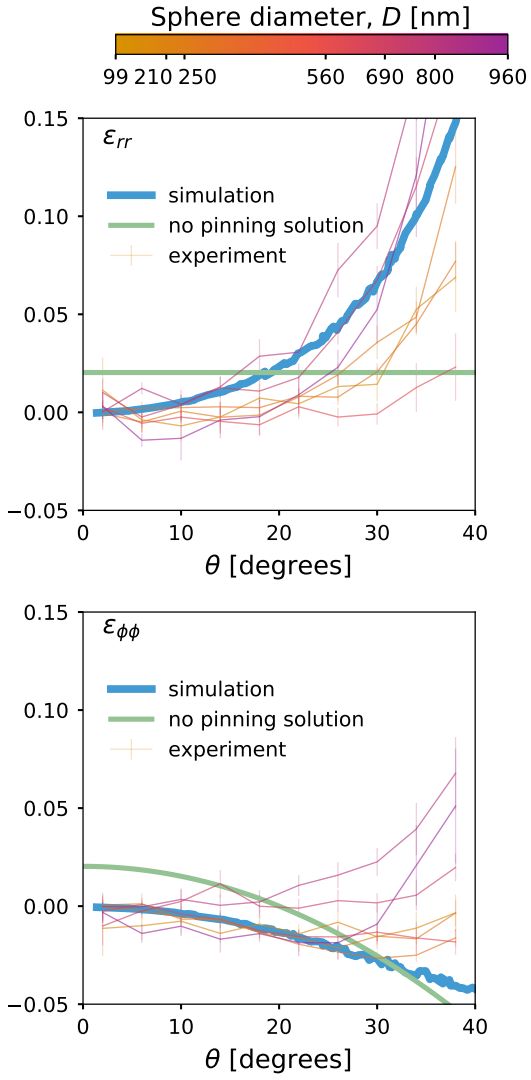

FIG. S4. **Strong pinning to the substrate is necessary for qualitative agreement with experiments.** The analytic solution in the case with no adhesion, given by the green curve, differs qualitatively from the simulation (blue curve) and experimental results (transparent orange and purple data).

Finite size effects in draped spring networks

We investigated the effects of finite size in the simulations of spring networks with respect to the substrate sphere size. Spring networks with lattice spacing a are draped over seven spheres in a triangular closed packed arrangement, as in Figure 1 of the main text. The resulting strains depend weakly on the ratio of sphere size to lattice spacing, D/a. While the shear and azimuthal strains are nearly unaffected by the size of the lattice up to down to values of $D/a \sim 6$, the radial strain begins to diverge significantly around $D/a \sim 10$. This is reminiscent of previous work on nanoparticle membranes [8], where the influence of the discrete lattice becomes significant for systems with a characteristic size of $\sim 10\,a$.

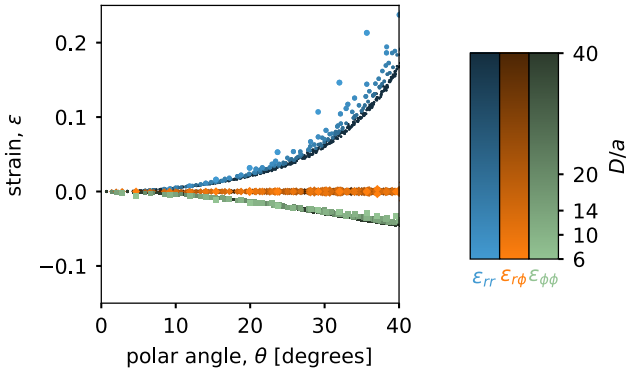

FIG. S5. **Finite size effects in the energetics of draped spring networks.** Spring networks with lattice spacing a were draped over seven spheres in a triangular closed packed arrangement, as in Figure 1 of the main text. The resulting strains depend only weakly on the ratio of sphere size to lattice spacing, D/a, so that the data coincide for all but the smallest values of D/a. While the shear and azimuthal strains are nearly unaffected by the size of the lattice, the radial strain begins to diverge significantly around $D/a \sim 10$.